

# NUMERICAL SIMULATION OF A PITCHING NACA 0012 AIRFOIL

Dipl.-Ing. Alexander Pechloff  
Lehrstuhl für Fluidmechanik\*, Technische Universität München

**Keywords:** *numerical simulation, Navier-Stokes equations, dynamic stall*

## Abstract

*This paper describes the application of the noncommercial CFD-code FLOWer to the problem of a sinusoidally pitching NACA 0012 airfoil with high amplitude and reduced frequency under incompressible flow conditions. As FLOWer allows the approximate solution of the nonlinear conservation laws governing viscous fluid flow, i. e. the Navier-Stokes equations, a numerical investigation of the unsteady boundary layer separation occurring during such a motion becomes feasible. Employing FLOWer under the incompressible conditions that correspond to the regarded experimental regime required an extensive preliminary analysis of the numerical parameters imbedded into the code. Having been primarily developed for transonic flow, it was possible to adjust FLOWer to the incompressible flow problem after studying the behavior of its various mechanisms for accelerating convergence and increasing stability. The necessary methodology to obtain optimal parameter settings was developed by critically examining steady state solutions at low angles of attack. The knowledge gained from these cases was then applied to simulate the sinusoidal movement of the NACA 0012 airfoil. FLOWer's accuracy in predicting the phenomena of the unsteady boundary layer separation was then assessed.*

## 1 Introduction

In the field of unsteady aerodynamics the term dynamic stall is frequently used to describe the complex fluid mechanical phenomena that occur

during extreme incidental movements of an airfoil beyond the angle of static stall. These processes are characterized by unsteady boundary layer separation, where a multitude of dynamic and viscous factors influence the flow field evolution. Extreme variations to the steady state flow separation become apparent. Initial investigations on this subject were performed in the sixties after stall induced rotor flutter had been observed during helicopter development. While in forward flight retreating rotor blades experience a combination of high incidences and low relative velocities of the oncoming freestream, resulting in an unsteady separated flow field in regions above the upper blade surface. With these dynamic phenomena having been localized as the cause for the flutter problem, further studies became necessary, as a means to extend the rotor's performance beyond the stall determined barrier.

A significant research breakthrough was achieved by confirming the existence of a distinct dynamic vortex structure on the suction side of the rotor blade. The use of an airfoil pitching in incidence allowed the reproduction of these physical effects under laboratory conditions for experimental analysis. Numerous measurement campaigns have been performed over the past years, in order to obtain and examine the dynamic stall evolution for a variety of wing and airfoil geometries, incidence motions and freestream conditions. Results are predominantly available for infinite wings based on the classic symmetrical rotor airfoils NACA 0015 and NACA 0012, with a sinusoidal incidence motion being imposed to simulate the cyclic blade pitch. Significant publications on this matter include the findings of Raffel, Kompenhans and Wernert [8] [10], pertaining to

---

\* Director: o. Prof. Dr.-Ing. Boris Laschka

a recent particle-image velocimetry campaign of the two-dimensional unsteady boundary layer separation above an oscillating airfoil. In accordance with [8] and [10] four sequential phases of the dynamic stall process can be discerned:

The initial phase is characterized by completely attached flow during the airfoil's upstroke motion, persisting even beyond the angle of static stall. As a distinguishing feature, a thin layer of reverse flow in proximity to the airfoil's surface becomes evident. At first occurring near the trailing edge, the layer quickly progresses towards the leading edge with increasing angle of attack, where it eventually initiates the so called dynamic stall vortex.

Development and progression of this leading edge vortex defines the second and most significant phase of the flow oscillation. With the deceleration of the reverse flow layer at the leading edge, unsteady boundary layer separation commences and the dynamic stall vortex is generated. As the incidence motion continues, the vortex increases in diameter and intensifies, subsequently moving downstream over the airfoil's surface. Because the vortex is in direct contact with the airfoil surface, the high circulation velocities result in a very pronounced, yet spatially limited zone of low pressure. This occurrence is responsible for maintaining high lift even after the primary suction peak at the leading edge collapses. In general maximum lift coefficients obtained during dynamic stall are significantly higher than their steady counterparts.

The previous phase concludes with the onset of post stall vortex shedding. As secondary vortex structures evolve near the leading and trailing edge under completely separated flow, the dynamic stall vortex detaches from the airfoil's surface and progresses into the wake. Consequently, the secondary suction peak induced by the dynamic stall vortex is no longer sustained, resulting in the collapse of the lift coefficient. These processes, which are associated with the downstroke motion of the airfoil, display a high degree of aperiodicity. Hence, a cycle to cycle

reproduction and acquisition of the phenomena is made difficult.

In the final phase of dynamic stall continuous flow reattachment occurs, beginning at the leading edge. The area of unseparated flow is repressed, with the remaining vortex structures dissolving into the wake. Reattachment is completed on the trailing edge towards the end of the downstroke.

At the Lehrstuhl für Fluidmechanik of the Technische Universität München research on the subject of dynamic stall has also been conducted, with Ranke [9] giving a universal definition for the two-dimensional unsteady boundary layer separation. The theories presented in [9] were applied to numerical methods and verified by Ranke through experiments performed on a sinusoidally pitching NACA 0012 airfoil with a reduced frequency of  $k_{red} = 0.3$  at  $Ma_\infty = 0.1$  and  $Re_\infty = 2.5 \cdot 10^5$ . The acquisition of this test case provided valuable reference data for future studies.

More recently research to extended this knowledge about the unsteady boundary layer separation to the third dimension has been underway. Unprecedented measurements to investigate the dynamic stall on an infinite swept wing with the above airfoil specifications for various reduced frequencies are to be supplemented by a database of numerical results for comparative studies. In the first phase a unsteady Navier-Stokes code is employed to simulate two-dimensional test cases and evaluate the accuracy of the numerically obtained flow fields. Unlike the coupling of unsteady boundary layer methods with inviscid outer flow solutions the use of a Navier-Stokes solver allows the computation of the flow field beyond the onset of the leading edge vortex, rendering the complete dynamic stall process and facilitating the analysis.

In the following chapters the numerical basics of the Navier-Stokes solver will be presented and its application to the dynamic stall scenario will be discussed. An extensive analysis of the numerical parameters allowed the adaptation of the code to the incompressible flow regime of the experimental test case, with

the evaluation of the simulation results also being given herein.

## 2 Basics of the Numerics

The numerical simulation of the sinusoidally pitching NACA 0012 airfoil is realized with the flow solver FLOWer, a noncommercial code developed by the German aerospace center (DLR), Daimler Chrysler Aerospace (DASA) and selected German universities for transonic flow around transport type aircraft. It is based on a finite volume discretization of the Reynolds-averaged Navier-Stokes equations, which are solved either in an explicit or implicit formulation using a multistage Runge-Kutta integration technique.

In general the explicit scheme is used to obtain initial steady state solutions before switching to the implicit scheme, allowing time accurate calculations for the unsteady case. This method, which is also known as dual time-stepping, circumvents the stability limitations imposed by the time increment of the explicit scheme.

A solution for an unsteady flow at a distinct moment in physical time results from the iterative determination of a pseudo steady state for that instant. The necessary pseudo time integration, however, allows the use of all stability enhancing and convergence accelerating methods of the explicit scheme, without sacrificing time accuracy. In this respect FLOWer offers such features as local time stepping, multigrid cycles, implicit residual averaging and adjustable artificial dissipation. The last feature ensues from the employed nondissipative finite volume discretization, which necessitates the introduction of artificial viscous terms for maintaining stability. The implemented Baldwin-Lomax turbulence model will be used in the following to simulate random flow fluctuations. A complete description of FLOWer's properties is given in [3], with fundamental algorithms having been derived by Kroll [4] and Radespiel [7].

## 2.1 Mathematical Model, Discretization and Stability

The Reynolds-averaged Navier-Stokes equations, governing the statistically treated unsteady viscous flow, can be written in conservative integral form as:

$$\frac{\partial}{\partial t} \iiint_V \bar{W} dV + \iint_{\partial V} (\bar{F}_c - \bar{F}_v) \bar{n} dS = 0 ; \quad (1)$$

$$\bar{W} = (\rho, \rho u, \rho v, \rho w, \rho E)^T$$

where  $\bar{W}$  denotes the solution vector containing the five unknown conservative variables: density  $\rho$ , the three Cartesian components of momentum  $\rho u$ ,  $\rho v$ ,  $\rho w$  and the total energy  $\rho E$ .  $V$  defines an arbitrary control volume, which is limited by its surface  $\partial V$ , with  $\bar{n}$  representing the normal vector of the control surface.  $\bar{F}_c$  and  $\bar{F}_v$  represent the tensors for the convective and viscous flux, respectively:

$$\bar{F}_c = \begin{bmatrix} \rho u \bar{e}_x + (\rho u^2 + p) \bar{e}_x + \rho v u \bar{e}_y + \rho w u \bar{e}_z \\ \rho v u \bar{e}_x + (\rho v^2 + p) \bar{e}_y + \rho w v \bar{e}_z \\ \rho w u \bar{e}_x + \rho w v \bar{e}_y + (\rho w^2 + p) \bar{e}_z \\ (\rho u E + u p) \bar{e}_x + (\rho v E + v p) \bar{e}_y + (\rho w E + w p) \bar{e}_z \end{bmatrix}, \quad (2)$$

$$\bar{F}_v = \begin{bmatrix} 0 \\ \sigma_{xx} \bar{e}_x + \sigma_{xy} \bar{e}_y + \sigma_{xz} \bar{e}_z \\ \sigma_{yx} \bar{e}_x + \sigma_{yy} \bar{e}_y + \sigma_{yz} \bar{e}_z \\ \sigma_{zx} \bar{e}_x + \sigma_{zy} \bar{e}_y + \sigma_{zz} \bar{e}_z \\ \bar{\Pi}_x + \bar{\Pi}_y + \bar{\Pi}_z \end{bmatrix} \quad (3)$$

with

$$\begin{aligned} \bar{\Pi}_x &= (u\sigma_{xx} + v\sigma_{xy} + w\sigma_{xz} - q_x) \bar{e}_x \\ \bar{\Pi}_y &= (u\sigma_{yx} + v\sigma_{yy} + w\sigma_{yz} - q_y) \bar{e}_y \\ \bar{\Pi}_z &= (u\sigma_{zx} + v\sigma_{zy} + w\sigma_{zz} - q_z) \bar{e}_z. \end{aligned} \quad (4)$$

The vectors  $\bar{e}_x$ ,  $\bar{e}_y$  and  $\bar{e}_z$  define the three Cartesian coordinate directions within the above

tensors. Pressure  $p$  is calculated with the thermal equation of state given as

$$p = (\kappa - 1) \rho \left( E - \frac{1}{2} (u^2 + v^2 + w^2) \right). \quad (5)$$

In equation (5)  $\kappa$  resembles the ratio of specific heats.

All components of the shear stress tensor  $\bar{\sigma}$  are governed by the material laws for Newtonian fluids under consideration of the Stokes hypothesis, while the components of the heat flux  $q_x$ ,  $q_y$  and  $q_z$  correspond to Fourier's law of heat conduction. Molecular viscosity is calculated according to Sutherland, whereas the heat conductivity results from the molecular viscosity  $\mu_L$  and the Prandtl number. In the case of turbulent flow the modeled eddy viscosity  $\mu_T$  is added to the molecular viscosity, just as the turbulent heat conductivity is added to the laminar one. For the sake of brevity these widely known equations will not be presented here, as they are detailed in [3]. This reference also includes information about the used algebraic turbulence model.

By employing a finite volume discretization based on central averaging to the Navier-Stokes equation (1) a system of ordinary differential equations is obtained with

$$\frac{d}{dt} \bar{W}_{i,j,k} = - \frac{1}{V_{i,j,k}} (\bar{R}_{i,j,k}^c - \bar{R}_{i,j,k}^v - \bar{D}_{i,j,k}), \quad (6)$$

allowing the calculation of the solution vector at each node of a structured grid. The right hand side of (6) contains the approximation of the convective and viscous fluxes  $(\bar{R}_{i,j,k}^c, \bar{R}_{i,j,k}^v)$  representing the net flux of mass, momentum and energy for a particular control volume  $V_{i,j,k}$  arrangement surrounding the grid node  $(i,j,k)$ .  $\bar{D}_{i,j,k}^c$  is the additional artificial term introduced into the equation, in order to dampen numerical oscillations induced by the solution process in the otherwise nondissipative scheme. The operator itself is comprised of a blend of second and fourth differences of the flow variables exercised within the semi-discrete system, in

order to preserve the conservation form. This technique was initially developed by Jameson [2]. A strict mathematical explanation of the operators mode of functioning has not been given. However, numerical experiments have shown that the method is very capable in producing stable solutions, especially in respect to viscous flow as Martinelli [5] describes.

Within FLOWer the user can exert control over the artificial viscous terms by adjusting the usually small parameter values of  $k^{(2)}$  and  $k^{(4)}$ . While the parameter  $k^{(2)}$  controls the first order dissipation introduced locally in shock vicinity,  $k^{(4)}$  sets the more general third order background dissipation applied to the global flow without discontinuities. For the incompressible flow regime, where no shocks are to be expected, the influence of the parameter  $k^{(4)}$  on the numerical solution has to be analyzed, whereas  $k^{(2)}$  can remain at its default setting of 1/2. Especially the trade off between stability and minimal solution distortion, resulting from too much artificial viscosity, has to be evaluated.

Besides adjusting the numerical dissipation the user retains the ability to control stability and convergence of the flow solution by adjusting the residual averaging algorithm implemented in FLOWer. For the three-dimensional computational domain the implicit and discretized smoothing equation is given as

$$(1 - \varepsilon_\xi \nabla_\xi \Delta_\xi) (1 - \varepsilon_\eta \nabla_\eta \Delta_\eta) (1 - \varepsilon_\zeta \nabla_\zeta \Delta_\zeta) \bar{P}_{i,j,k}^{(m)} = \bar{P}_{i,j,k}^{(m)}, \quad (7)$$

where  $\bar{P}_{i,j,k}^{(m)}$  denotes the  $m$ -th stage residual vector of the multistage Runge-Kutta scheme, as applied to the ordinary differential equation (6). Within the factorized averaging equation (7)  $\nabla$  and  $\Delta$  represent the normal forward and backward difference operators, respectively, whereas  $\varepsilon_\xi$ ,  $\varepsilon_\eta$  and  $\varepsilon_\zeta$  are the positive smoothing coefficients in the individual coordinate directions. In studies presented here only  $\varepsilon_{xyz} = \varepsilon_\xi = \varepsilon_\eta = \varepsilon_\zeta$  will be examined. The averaged residual vector  $\bar{P}_{i,j,k}^{(m)}$  results from the iterative solution of equation (7) at distinct Runge-Kutta

stages. By employing this technique the allowable time increment of the integration process can be extended far beyond the actual stability limit. The user has two possibilities to adjust this feature to the individual flow problem, by setting either constant or adaptive smoothing coefficients.

The first method presents a simple way of dampening numerical instabilities. According to Martinelli [5] optimizing the smoothing coefficients for a certain test case requires a certain degree of experience, in order to obtain the desired convergence behavior. However, the required numerical investigations for determining these empirical coefficients can become quite extensive.

In contrast the adaptive form of implicit residual averaging uses smoothing coefficients that are a function of the local characteristic wave speeds in the individual cell. The user exerts control on the algorithm by defining an interval for the lower and upper value of the allowed smoothing coefficient. For this method the user once again has to obtain knowledge about the selected test case's stability behavior, somewhat limiting the adaptive techniques advantages. Regardless of the chosen technique the optimization of the implicit residual averaging is prerequisite to obtaining stable Navier-Stokes solutions. Especially the cell volumes of high aspect ratio, as employed in the resolution of boundary layer gradients, limit the allowed time increment and define the stability region of the scheme.

The discretization of the physical domain surrounding the airfoil is accomplished with a two-dimensional single block structured grid based upon a 'C-topology' as depicted in Fig. 1. Elliptical smoothing of the grid was performed, in order to satisfy FLOWer's requirement of second-order accurate spatial discretization. The airfoil's contour is digitized with 257 individual points. In preliminary investigations the grid was composed of  $384 \times 64$  cells, with the first grid line's off-body distance being  $0.9 \cdot 10^{-3}$  chord lengths. Numerical studies revealed, however, that this discretization was insufficient in resolving the boundary layer properly. Hence,

the number of cells was increased to  $384 \times 96$ , while the off-body distance was reduced to  $0.5 \cdot 10^{-3}$  chord lengths. Fig. 2 depicts the resolution of the  $384 \times 96$  grid in proximity to the airfoil surface. The results presented in this paper all pertain to this grid.

In the following a small excerpt of the extensive numerical studies performed with FLOWer on turbulent steady state cases with low angles of attack ( $Ma_\infty = 0.1$ ,  $Re_\infty = 2.5 \cdot 10^5$ ) will be given. The analysis of FLOWer's behavior regarding convergence acceleration techniques such as local time stepping and multigrid cycles can be reviewed in Pechloff [6]. The results for the implicit residual averaging and artificial dissipation however are discussed.

## 2.2 Evaluation of the Implicit Residual Averaging

The initial motive for studying the implicit residual averaging evolved during the transition from the  $384 \times 64$  grid to the finer  $384 \times 96$  grid, due to the integration scheme exhibiting extreme sensitivity to the higher resolution of the boundary layer. Previous calculations on the coarse grid performed beyond FLOWer's theoretical stability limit of  $CFL = 3.75$  (Courant-Friedrich-Levy number) [5] showed adequate convergence and stability with FLOWer's default setting of the smoothing coefficient  $\epsilon_{xyz} = 0.7$ . Attaining a stable steady state solution with the finer mesh, however, was no longer possible with this setting, with a shift of the integration algorithm's region of stability having become evident. In order to determine the new  $\epsilon_{xyz}$  parameter values for residual averaging with constant coefficients, the stability region in respect to different CFL-numbers (3.75, 5.625 and 7.5) was examined. As the user exerts control over the integration algorithm's time increment by setting the CFL parameter, it becomes necessary to adjust the residual averaging accordingly.

Criterion for localizing the  $\epsilon_{xyz}$  interval is the convergence of the steady state solution below a root mean squared (RMS) density

residual of  $1.0 \cdot 10^{-5}$ , after which the calculation is terminated. Reaching a limit of 1500 multigrid cycles is defined as the secondary criterion. Beyond this limit a solution will be classified as not convergent. Settings for the multigrid cycle were optimized in preliminary investigations not presented here and remained unmodified in the course of this evaluation. It should be noted that a ‘symmetrical W’ multigrid cycle type had been found to be very efficient for convergence acceleration.

Evaluating the implicit smoothing algorithm’s behavior, as performed in Fig. 3, a distinct boundary of convergence for each variation of the CFL number becomes obvious and presents a specific interval for the setting of the respective smoothing coefficient  $\varepsilon_{xyz}$ . Furthermore within each stability region an optimal value for the smoothing coefficient exists, accomplishing convergence down to engineering accuracy with a minimum amount of multigrid cycles. Regarding the optimal smoothing coefficient for each individual CFL-number, a reduction in computational effort by 9% can be realized when increasing the CFL-number from 3.75 to 7.5. The results of the evaluation are especially interesting for the adaptive form of implicit residual averaging, because it is now possible to properly set the upper and lower boundary of the smoothing coefficient’s interval in respect to the CFL-number.

As the increase of the NACA 0012 airfoil’s angle of attack is in general associated with a deterioration in convergence behavior, it can be expected that the convergence boundaries obtained for  $\alpha = 0^\circ$  will constrict, thus reducing the allowed coefficient interval for the adaptive smoothing algorithm. Consequently, without resetting the interval boundaries the amount of multigrid cycles required to breach the residual tolerance level would continuously increase, up to the point where a steady state solution can no longer be attained. In regards to the unsteady simulation of an incidence motion, such as will be presented in later chapters, a perpetual manual adjustment of the adaptive interval would become necessary.

A comparison of the constant coefficient smoothing algorithm at optimal settings ( $\varepsilon_{xyz} = 1.9$ ,  $CFL = 7.5$ ) with the adaptive one limited to the stability region favors the first method in respect to convergence behavior (Fig. 4). Hence, under incompressible flow conditions the method of adaptive residual averaging is deemed not as effective as the constant coefficient technique once the optimal setting has been retrieved. This result remains in discrepancy with the effectiveness of the adaptive technique as described in Radespiel [7]. To which extent the residual averaging distorts the solution was not examined in this study.

### 2.3 Influence of the Artificial Viscosity

As was mentioned in chapter 2.1, the user is able to control the amount of background viscosity artificially introduced into the solution by setting the parameter  $k^{(4)}$ . However, this has to be done very cautiously, because the stability enhancing feature of the artificial dissipation comes with a trade off in regards to solution accuracy. In order to obtain an optimal setting for the third order dissipative constant  $k^{(4)}$  one has to examine stability behavior and deviation of the solution from the physical flow.

The first study investigates the effect of a  $k^{(4)}$  variation on the convergence behavior of the calculation. Once again steady state solutions at  $\alpha = 0^\circ$  are examined, with the CFL-number and constant smoothing coefficient set to  $CFL = 7.5$  and  $\varepsilon_{xyz} = 1.9$ , respectively, as a result of the previous evaluation (chapter 2.2). In accordance, steady state calculations are terminated either after reaching a RMS density residual smaller than  $1.0 \cdot 10^{-5}$  or exceeding 1500 multigrid cycles. Variation of the dissipation constant  $k^{(4)}$  was performed by successively halving the default value of  $1/64$  as a means of decreasing dissipation levels. On the other hand an increase in background dissipation was achieved by successively doubling this initial value. Results of this study are depicted in Fig. 5. As a principal observation it can be stated that the increase in artificial background dissipation leads to an accelerated convergence

and vice versa. This behavior is a direct consequence of the stabilization quantity introduced into the solution algorithm. With a setting of  $k^{(4)} = 1/16$  fastest convergence to the steady state solution is achieved, requiring only 298 multigrid cycles and exhibiting minimal oscillations in the density residual's progression. In contrast the reduction of  $k^{(4)}$  to  $1/512$  requires 1285 multigrid cycles to achieve the specified tolerance level, while showing greater oscillations in the residual.

The behavior of the calculation at the two boundaries of the convergence region is also quite different. Further increase of  $k^{(4)}$  from  $1/16$  to  $1/8$  leads to a sudden convergence limit, with the cause being identified as local instabilities of the algorithm occurring near the airfoil's leading edge. Continued reduction of the background dissipation to a minimal value, however, leads to an asymptotic progression of the residual towards the specified accuracy. Therefore the lower convergence boundary for  $k^{(4)}$  is determined by the global destabilization of the solution, with termination occurring after the maximum amount of multigrid cycles. Even though rapid convergence can be achieved through a setting of  $k^{(4)} = 1/16$ , the quality of the solution has to be regarded as a second criterion before deciding on an optimal setting.

Because the introduction of the artificial viscous terms has a similar effect in dampening numerical oscillations and accelerating convergence as the implicit residual averaging, the relationship between these two methods has to be examined first. This is accomplished by localizing the boundary of convergence in regards to the smoothing coefficient  $\epsilon_{xyz}$  for each variation of the third order dissipation constant  $k^{(4)}$ . The methodology is equivalent to the one described in chapter 2.2, but performed for a  $2^\circ$  airfoil incidence. As becomes evident in Fig. 6 an increase of the third order dissipation constant leads to a broadening of the allowable smoothing interval. Hence, the parameter  $\epsilon_{xyz}$  doesn't require an optimal setting as a means to achieve adequate convergence behavior, because solution stability is increasingly supplied by  $k^{(4)}$ . In the most extreme case of  $k^{(4)} = 1/16$  a

smoothing interval between 1.5 and 2.1 for  $\epsilon_{xyz}$  is still sufficient to obtain the specified residual tolerance. Complementary to this behavior a continuous reduction of dissipation levels makes the integration algorithm more sensitive towards the implicit residual averaging. As a consequence either the employed smoothing coefficient or the adaptive interval have to be set meticulously as a means of stabilizing the calculation.

Finally the aspect of solution distortion is analyzed by observing the drag coefficient's variation in relation to the applied stabilization methods. Results are depicted in Fig. 7. Implicit residual averaging for a fixed level of background dissipation portrays hardly any influence on the airfoil's drag coefficient  $C_d$ . On the other hand variation in the third order dissipation constant has significant impact on  $C_d$ , which is inherently coupled with the flow's viscosity. A minimal drag coefficient for  $k^{(4)} = 1/32$  within the interval of  $1/16$  and  $1/512$  becomes evident. Because of the artificial dissipative terms introduced into the discretized equation (6), the solution in general tends to have a higher degree of viscosity than the actual physical flow. Hence, by localizing the minimum of the drag coefficient it can be argued, that a setting of  $k^{(4)} = 1/32$  achieves a solution with the least distortion, with  $C_d$  being closest to the actual physical value. Under consideration of the stabilizing and convergence accelerating effects of the numerical background dissipation, a setting of  $k^{(4)} = 1/32$  is deemed optimal for approximating physically accurate solutions.

### 3 Unsteady Simulation

#### 3.1 Method

To validate FLOWer's ability to properly predict the occurring unsteady flow phenomena associated with deep dynamic stall a sinusoidal pitching motion corresponding with the experimental test case supplied by Ranke [9] ( $Ma_\infty = 0.1$ ,  $Re_\infty = 2.5 \cdot 10^5$ ) was conducted. The incidence law given by

$$\alpha(t) = 10^\circ - 10^\circ \cdot \cos(2\pi f \cdot t) \quad (8)$$

governs an airfoil motion that consist of a  $\pm 10^\circ$  incidence variation about a mean incidence of  $10^\circ$ , with the pitching axis located at 25% chord length from the leading edge. The values of frequency  $f = 2.0$  Hz, freestream velocity  $U_\infty = 12.6 \text{ ms}^{-1}$  and chord length  $c = 0.3$  m lead to a reduced frequency of

$$k_{red} = \frac{2\pi f c}{U_\infty} \approx 0.30. \quad (9)$$

Employing FLOWer's dual time stepping algorithmn, a Navier-Stokes simulation of the motion defined by (8) can be accomplished after supplying an initial steady state solution. In this case a steady state solution of the oscillation's lower dead center was used, which was obtained through the application of methods described in chapters 2.2 and 2.3. A single period of oscillation ( $T$ ) is discretized with 100 individual time steps, each being the equivalent of  $\Delta t/T = 0.01$  nondimensional phase increments. In order to eliminate transient phenomena from the solutions, oscillations beyond the initial cycle will have to be completed.

Regarding the numerics, parameter settings respective to multigrid, local time stepping, implicit residual averaging and dissipation are taken from the steady state solution and transferred to the dual time stepping scheme. Because FLOWer calculates a pseudo steady state for each physical time step, it was able to achieve satisfying results by using this method. However, the tolerance for the RMS density residual had to be raised to  $1.2 \cdot 10^{-5}$  over the entire oscillation, as a means of terminating the calculation at each instance. During the phase of dynamic stall vortex shedding convergence to this specified accuracy was not attainable, due to the highly unsteady nature of the occurring flow field and the size of the selected time increment. For these solutions the convergence of the integral coefficients such as lift  $C_l$ , drag  $C_d$  and moment  $C_m$  had to be observed, in order to determine if the pseudo steady state had been reached. The maximum amount of pseudo-iterations was limited to 150 multigrid cycles.

The results presented in the following chapter relate to the  $384 \times 96$  grid, with no grid deformation occurring over the incidence motion, as FLOWer adjusts the boundary conditions accordingly.

## 3.2 Description and Discussion of Results

To denote up- and downstroke the symbols  $\uparrow$  and  $\downarrow$  are introduced, respectively. Labels contained in figures are referred to by  $\{\mathbf{x}\}$ . Flow fields are visualized through the total velocity  $u_{tot}$ .

### 3.2.1 Evaluation of the Lift Coefficient $C_l$ over the Incidence Angle $\alpha$

As becomes evident in **Fig. 8**, significant transient phenomena is eliminated after six complete cycles of the sinusoidal pitching motion. Even though good reproducibility of the lift coefficient can be obtained for the upward stroke, strong aperiodic effects can be observed during the downward motion, attributable to the vortex shedding occurring beyond  $19.30^\circ \downarrow$  incidence ( $t/T = 0.56$  **{C}**). However, it still remains to be seen if the aperiodic effects encountered during the downstroke are primarily a chaotic phenomena or are the result of a cycle dependent phase shift, as cycles two and four would indicate. The ascending branch of the hysteresis is predominated by attached flow, with the thin reverse flow layer first appearing at  $10.63^\circ \uparrow$  ( $t/T = 0.26$ ) and reaching the leading edge at  $19.30^\circ \uparrow$  ( $t/T = 0.44$  **{B}**). At this instance the dynamic stall vortex is induced, its evolution and intensification leading to a maximum lift coefficient of  $C_{l \max} = 2.015$  during the downstroke ( $19.69^\circ \downarrow$ ,  $t/T = 0.54$ ).

Within the next two time increments ( $19.69^\circ \downarrow$ ,  $t/T = 0.54$ ) the lift collapses, as a new vortex evolves in proximity to the trailing edge, progressively separating the dynamic stall vortex from the airfoil surface. The subsequent reattachment of the dynamic stall vortex during the first half of the downward motion results in a secondary maximum lift coefficient of  $C_{l \max 2} = 0.471$  ( $13.09^\circ \downarrow$ ,  $t/T = 0.70$ ), being preceded by a minimum lift coefficient of  $C_{l \min} = -0.002$  ( $14.82^\circ \downarrow$ ,  $t/T = 0.67$ ). The onset of flow

reattachment can be localized at an incidence of  $11.87^\circ \downarrow$  ( $t/T = 0.72$  {D}).

### 3.2.2 Evaluation of the Pressure Coefficient Variation $C_p$ over the Incidence Angle $\alpha$ and of Selected Flow Fields

From the  $C_p$ - $\alpha$ - $x/c$  contours depicted in **Fig. 9** and **10** eight significant properties of the dynamic stall process can be extracted. Labels used in this context refer exclusively to these two figures. The upward motion of the airfoil, which is predominated by attached flow, is characterized by the development of a primary suction peak above the leading edge {1} ( $C_{p_{min}} = -10.2$ ,  $18.76^\circ \uparrow$ ,  $t/T = 0.42$ ). This results from high flow velocities occurring as fluid passes around the airfoil's leading edge. After the appearance of the dynamic stall vortex {2} ( $19.30^\circ \uparrow$ ,  $t/T = 0.44$ , **Fig. 11**) and its development (**Fig. 12**), which has a circulation center located horizontally at approximately 25% chord length, the leading edge pressure formation collapses. The cause for this process is identified in the intensification and expansion of the dynamic stall vortex, detaching the flow around the leading edge.

Behavior of the pressure coefficient during this upward motion corresponds well with results from Coton [1], who performed so called ramp-up experiments with airfoils pertaining to dynamic stall. Even though a linear incidence law with a constant maximum angle governed the airfoil motion, a similar drop in the primary suction peak was observed after the inception of the leading edge vortex. Coton having acquired data for a nonperiodic flow, however, further comparisons of the  $C_p$ - $\alpha$ - $x/c$  distributions are not possible.

Returning to the sinusoidally pitching airfoil, the secondary suction bulge, which is induced by the dynamic stall vortex, achieves its minimum value of  $C_{p_{min2}} = -5.2$  {2} at an incidence of  $19.82^\circ \uparrow$  ( $t/T = 0.47$ ). At this point the vortex has reached its maximum circulation intensity, which will steadily decrease as the vortex moves downstream and continues to expand. While the primary suction peak reduces during the downward motion {3}, the dynamic stall vortex as characterized by the secondary

suction bulge passes over the airfoil surface towards the trailing edge {4}. It becomes evident, that the secondary suction effect, which is primarily responsible for maintaining high lift, decreases with the progression of the pitching motion. At the same instance, however, the vortex induced area of low pressure extends farther across the airfoil surface, consequently shifting the moment of maximum lift  $C_{l_{max}} = 2.015$  into the downstroke ( $19.69^\circ \downarrow$ ,  $t/T = 0.54$ ). In this respect **Fig. 13** shows the dynamic stall vortex at an incidence of  $19.30^\circ \downarrow$  ( $t/T = 0.56$ ), having reached its largest diameter and extending over approximately 75% of the airfoil's chord length.

With the subsequent shedding of the dynamic stall vortex, the suction ridge {4} subsides and gives way to a new low pressure peak forming at the trailing edge {5}. It is induced by the evolution of the trailing edge vortex, which gains on influence during the downward motion before drifting into the wake. As a result the trailing edge suction peak diminishes {6}, coinciding with the reattachment of the dynamic stall vortex to the airfoil surface (**Fig. 14**) and the renewed induction of a low pressure area {7}. These two characteristics correspond with the above mentioned minimum  $C_{l_{min}} = -0.002$  and secondary maximum  $C_{l_{max2}} = 0.471$  of the lift coefficient, occurring at  $14.82^\circ \downarrow$  ( $t/T = 0.67$ ) and  $13.09^\circ \downarrow$  ( $t/T = 0.70$ ) respectively.

The phase of flow reattachment features a smoothed contour, as primary and secondary vortex structures no longer have any effect on the airfoil's pressure distribution. With reattachment of the flow starting at the leading edge, a renewed build up of the primary suction peak can be observed {8}. However, the completion of the downstroke leads to its reduction, as the incidence angle decreases and the initial state of flow is reached at the motion's lower dead center.

### 3.2.3 Resume

Comparing the numerical results with the corresponding experimental test case acquired by Ranke [9] showed good conformity in the phenomenology. The onset of the thin reverse

flow layer, the development of the dynamic stall vortex, post stall vortex shedding and flow reattachment occurred within  $\Delta t/T \approx \pm 0.03$  non-dimensional phase increments pertaining to the experimental values. Simulated phenomena during the phase of aperiodic vortex shedding, such as secondary vortex structures, are in good qualitative agreement with particle image velocimetry data obtained by Raffel [8] and Wernert [10], using a somewhat modified incidence law. After FLOWer's adaptation to the incompressible flow regime, its ability to properly predict the unsteady boundary layer separation has been successfully evaluated and established.

In order to determine the effect of the time increment on the Navier-Stokes solution the previously used time step size is halved to  $\Delta t/T = 0.005$  and the computation of the pitching cycle repeated. Consequently, the sinusoidal pitching motion is now discretized in 200 individual time steps. Comparison of the lift coefficients development over the incidence for both cases, as depicted in Fig. 15, shows no influence of the time step size up to the point where maximum lift occurs and post stall vortex shedding commences. Beyond this mark the lift coefficient for the new computations does not reproduce, but nonetheless returns a curve with similar local characteristics, such as the secondary lift maximum. This divergent behavior can be attributed to the strong aperiodic effects persistent throughout the vortex shedding phase, which are especially sensitive to the chosen time step.

#### 4 Conclusions

By analyzing the behavior of the Navier-Stokes solver FLOWer in regards to its stability enhancing and convergence accelerating features, parameter settings for incompressible flow conditions were determined. The obtained steady state solution was used as a starting point for unsteady simulations of the pitching NACA 0012 airfoil. FLOWer's ability to predict the phenomenology of the two-dimensional deep dynamic stall process was validated by simulating an acquired experimental test case. The

results and insight gained through methodology and calculations received further application during quasi-three-dimensional computations of the unsteady boundary layer separation on an infinite swept wing.

#### References

- [1] Coton, F.N., Galbraith, R.A.McD., Jiang, D. and Gilmour, R.: *An experimental study of the effect of pitch rate on the dynamic stall of a finite wing*. Department of Aerospace Engineering, University of Glasgow, Glasgow: G12 8QQ, 1996
- [2] Jameson, A., Schmidt W. and Turkel, E.: *Numerical solutions of the Euler equations by finite-volume methods using Runge-Kutta time-stepping schemes*. AIAA 81-1259, 1981
- [3] Kroll, N.: *FLOWer - Installation and user handbook Version 114/115*. Deutsche Forschungsanstalt für Luft- und Raumfahrt e.V., Institut für Entwurfsaerodynamik, 1997-1998
- [4] Kroll, N. and Jain, R.K.: *Solution of two-dimensional Euler equations - experience with a finite volume code*. Braunschweig: DFVLR-FB 87-41, 1987
- [5] Martinelli, L. and Jameson, A.: *Validation of a multigrid method for the Reynolds averaged equations*. University of Princeton, Department of Mechanical and Aerospace Engineering: AIAA Paper 88-0414, 1988
- [6] Pechloff, A.: *Numerische Simulation eines schwingenden und schiebenden NACA0012 Flügels unter Anwendung des Navier-Stokes-Lösers FLOWer*. Technische Universität München, Lehrstuhl für Fluidmechanik, Diplomarbeit, 1998
- [7] Radespiel, R. and Rossow, C.: *Efficient cell-vertex multigrid scheme for the three-dimensional Navier-Stokes equations*. Institute for Design Aerodynamics, Federal Republic of Germany: *AIAA Journal*, Vol. 28, No. 8, 1990
- [8] Raffel, M., Kompenhans, J., Wernert P.: *Investigation of the unsteady flow velocity field above an airfoil pitching under deep dynamic stall conditions*. DLR, German Aerospace Research Establishment, D-37073, Göttingen, Germany: *Experiments in Fluids*, Springer Verlag, 1995
- [9] Ranke, H.: *Instationäre Grenzschichtablösung in ebener inkompressibler Strömung*. Technische Universität München, Lehrstuhl für Fluidmechanik, Dissertation, 1994
- [10] Wernert, P., Geissler, W., Raffel, M. and Kompenhans J.: *Experimental and numerical investigations of dynamic stall on a pitching airfoil*. DLR, German Aerospace Research Establishment, D-37073, Göttingen, Germany: *AIAA Journal*, Vol. 34, No. 8, 1996

Figures

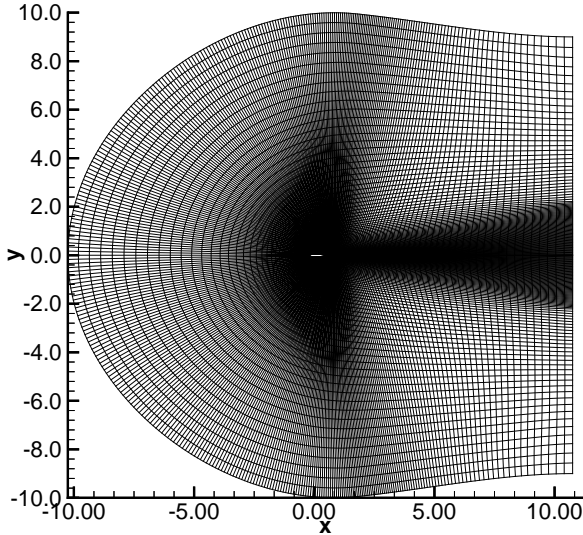


Fig. 1. 384 × 96 'C-topology' grid

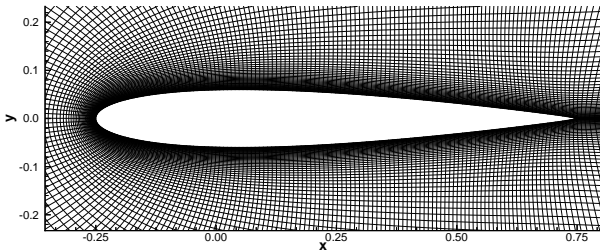


Fig. 2. Mesh structure in airfoil proximity

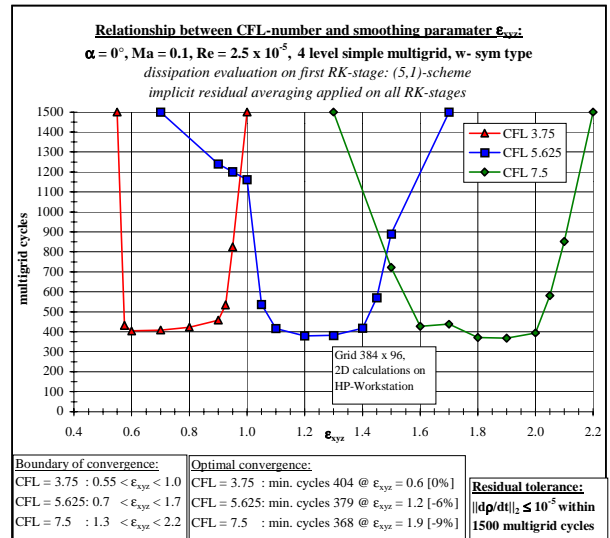


Fig. 3. CFL-number dependent boundaries of convergence

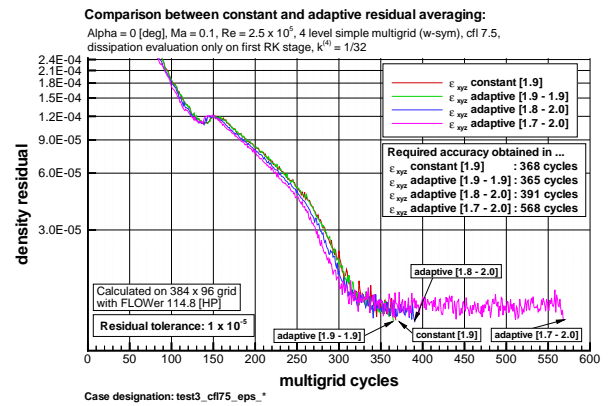


Fig. 4. Comparison of the residual averaging techniques

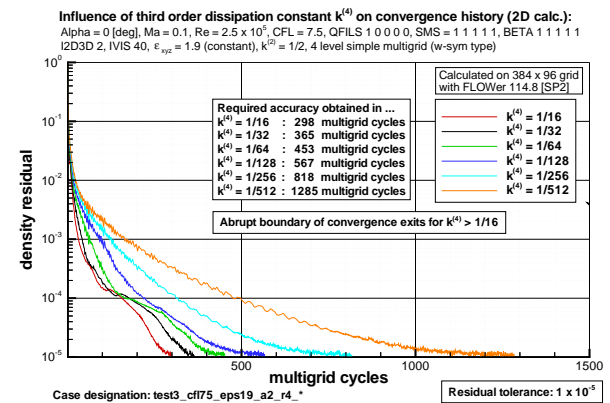


Fig. 5. Influence of third order background dissipation

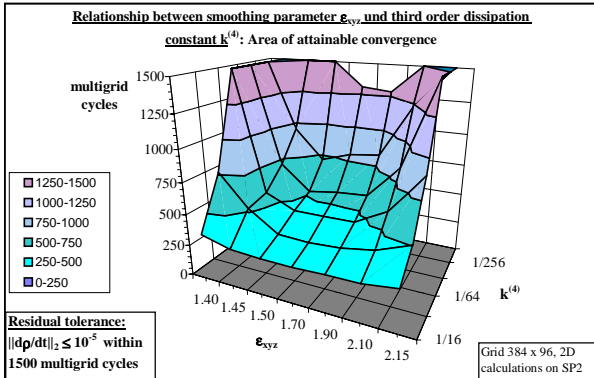


Fig. 6. Convergence area obtained for  $\epsilon_{xyz}$  and  $k^{(4)}$  variation

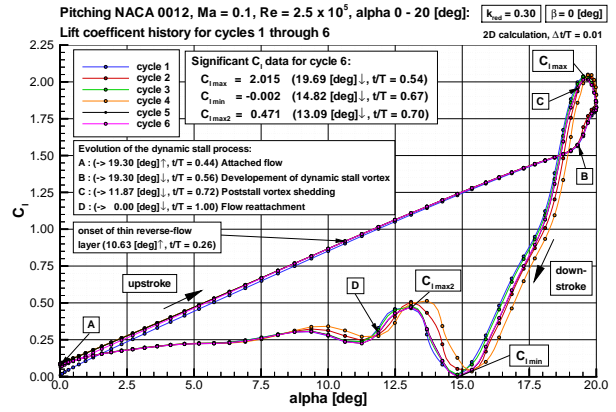


Fig. 8. Lift coefficient over incidence ( $k_{red} = 0.30$ ,  $\Delta t/T = 0.01$ )

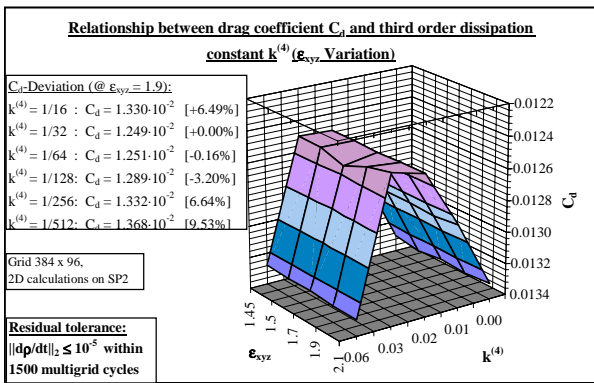


Fig. 7. Influence of  $k^{(4)}$  on the drag coefficient  $C_d$

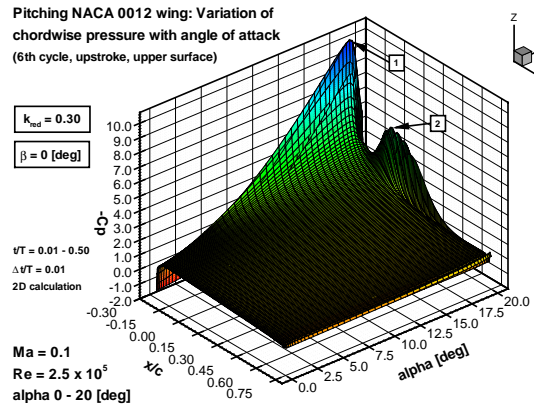


Fig. 9.  $C_p$ - $\alpha$ - $x/c$ -contour ( $k_{red} = 0.30$ , upstroke)

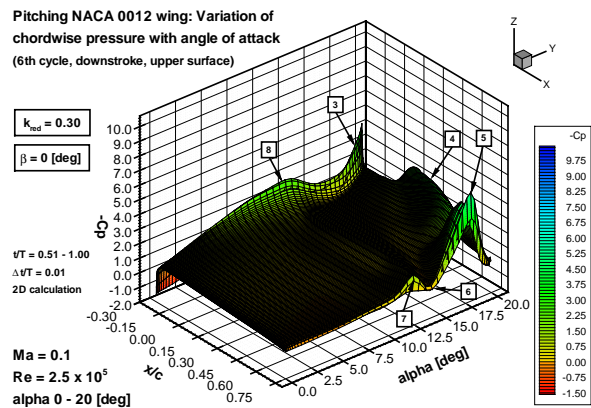


Fig. 10.  $C_p$ - $\alpha$ - $x/c$ -contour ( $k_{red} = 0.30$ , downstroke)

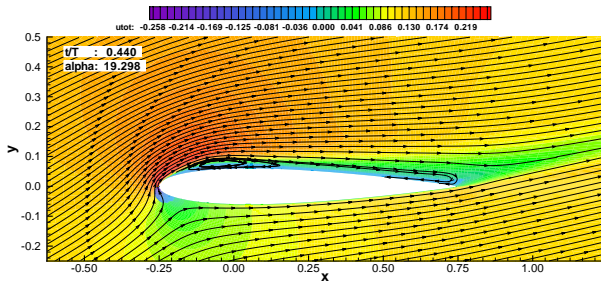


Fig. 11. Flow field ( $k_{red} = 0.30$ ,  $\alpha = 19.30^\circ \uparrow$ ,  $t/T = 0.44$ )

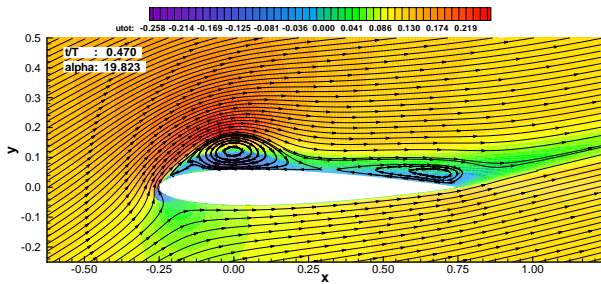


Fig. 12. Flow field ( $k_{red} = 0.30$ ,  $\alpha = 19.82^\circ \uparrow$ ,  $t/T = 0.47$ )

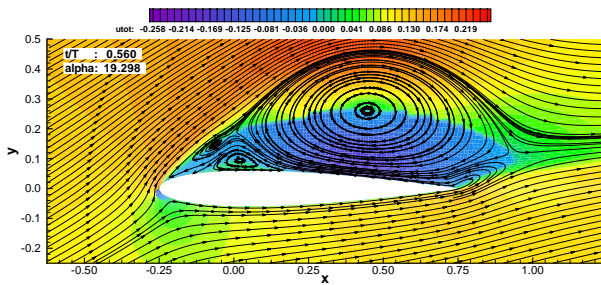


Fig. 13. Flow field ( $k_{red} = 0.30$ ,  $\alpha = 19.30^\circ \downarrow$ ,  $t/T = 0.56$ )

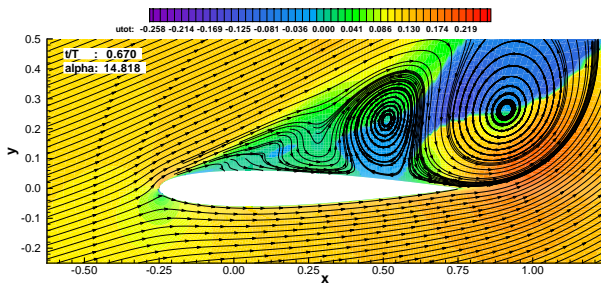


Fig. 14. Flow field ( $k_{red} = 0.30$ ,  $\alpha = 14.82^\circ \downarrow$ ,  $t/T = 0.67$ )

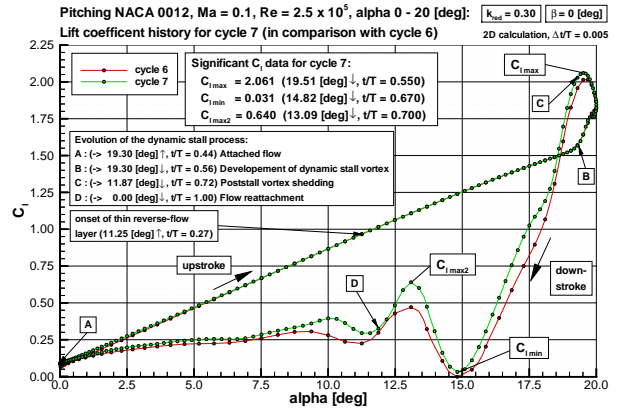


Fig. 15. Lift coefficient over incidence ( $k_{red} = 0.30$ ,  $\Delta t/T = 0.005$ )